

Self-Consistent Grain Size Evolution controls Strain Localization during Rifting

Jonas Ruh (✉ jonas.ruh@erdw.ethz.ch)

ETH Zurich

Leif Tokle

ETH Zurich

Whitney Behr

ETH Zürich

Article

Keywords: tectonic, mantle dynamics, geodynamic numerical models, rifting

Posted Date: June 22nd, 2021

DOI: <https://doi.org/10.21203/rs.3.rs-561920/v1>

License: © ⓘ This work is licensed under a Creative Commons Attribution 4.0 International License.

[Read Full License](#)

Version of Record: A version of this preprint was published at Nature Geoscience on June 16th, 2022. See the published version at <https://doi.org/10.1038/s41561-022-00964-9>.

1 **Self-Consistent Grain Size Evolution controls Strain Localization during Rifting**

2

3 **J. B. Ruh^{1*}, L. Tökle¹, and W. M. Behr¹**

4 ¹Structural Geology and Tectonics group, Geological Institute, Department of Earth Sciences,

5 ETH Zürich, Switzerland

6

7 *Corresponding author: Jonas B. Ruh (jonas.ruh@erdw.ethz.ch)

8

9 **Key Points:**

- 10
- Self-consistent grain size evolution according to the paleowattmeter is coupled to a 2D

11 thermo-mechanical numerical model of the upper mantle

 - Mantle rheology is represented by a coupled grain-size-dependent diffusion and grain-

12 size-independent dislocation creep flow law

 - Strain localization along lithospheric shear zones leads to reduced grain sizes and

13

14

15 diffusion creep becomes the dominant deformation mechanism

16 **Abstract**

17 Geodynamic numerical models often employ solely grain-size-independent dislocation
18 creep to describe upper mantle dynamics. However, observations from nature and rock
19 deformation experiments suggest that shear zones can transition to a grain-size-dependent creep
20 mechanism due to dynamic grain size evolution, with important implications for the overall
21 strength of plate boundaries. We apply a two-dimensional thermo-mechanical numerical model
22 with a composite diffusion-dislocation creep rheology coupled to a dynamic grain size evolution
23 model based on the paleowattmeter. Results indicate average olivine grain sizes of 3–12 cm for
24 the upper mantle below the LAB, while in the lithosphere grain size ranges from 0.3–3 mm at the
25 Moho to 6–15 cm at the LAB. Such a grain size distribution results in dislocation creep being the
26 dominant deformation mechanism in the upper mantle. However, deformation-related grain size
27 reduction below 100 μm activates diffusion creep along lithospheric-scale shear zones during
28 rifting, affecting the overall strength of tectonic plate boundaries.

29

30 **Main**

31 The Earth's lithosphere is defined by its mechanically rigid behavior in contrast to the
32 relatively weak underlying asthenosphere. This rheological stratification, which ultimately
33 allowed for the emergence of plate tectonics, primarily results from the apparent thermal gradient
34 across the crust and upper mantle and the temperature-dependent activation of dislocation- and
35 diffusion-related crystal-plastic creep of rocks and minerals^{1,2}. Scaling of such experimentally-
36 derived creep laws to natural strain rates allows us to estimate viscosities and strength of the
37 lithosphere. Geophysical constraints on the elastic thickness of the continental lithosphere, that is
38 a proxy for its strength³, led to contrasting conclusions on the uppermost mantle being either

39 strong and best represented by dry dislocation creep of olivine⁴ or weak according to a wet
40 olivine rheology^{5,6}.

41 Whether deformation within the upper mantle is dominated by dislocation creep or
42 diffusion creep is still a matter of debate. The observation of crystallographic preferred
43 orientation (CPO) in mantle xenoliths⁷ and evidence of strong seismic anisotropy⁸ has long been
44 interpreted as an indicator for dislocation creep as the dominant deformation mechanism¹.
45 However, there is reported evidence that CPO, and therefore seismic anisotropy, may also
46 develop as a result of diffusion creep of olivine-rich aggregates^{9,10}. In contrast to dislocation
47 creep, the relationship between stress and strain rate for diffusion creep is dependent on grain
48 size, which is a crucial parameter when considering the dominant deformation mechanism in the
49 upper mantle¹¹⁻¹⁴. A transition from dislocation to diffusion creep at depths greater than ~250 km
50 was proposed by Hirth and Kohlstedt¹² based on theoretical estimations that olivine grain size in
51 the upper mantle is on the order of 10 mm¹⁵. Numerical experiments of mantle convection have
52 since implemented a composite diffusion-dislocation creep rheology and constant mantle grain
53 size, which may result in dramatic convective instability and thermal erosion of the lithosphere¹⁶.
54 However, the assumption of a constant upper mantle grain size is an oversimplification that
55 appears contradictory to several observational and experimental datasets. Experimental data on
56 wave speed and attenuation of olivine, for example, fits best with a seismological model that
57 implies an increase in grain size from ~1 mm to ~5 cm between depths of 100–200 km¹⁷.
58 Furthermore, natural samples of exhumed lithospheric mantle rocks show a large variety of grain
59 sizes ranging from tens to hundreds of microns in olivine mylonites and tectonites to the
60 centimeter-scale in weakly deformed or annealed xenoliths¹⁸⁻²¹.

61 Active plate tectonics requires mechanical weakening and strain localization along
62 lithospheric shear zones at the plate boundaries^{22,23}. Several studies suggest that grain size
63 reduction and the consequent activation of diffusion creep is a viable process to initiate
64 localization of deformation in the lithosphere²⁴⁻²⁹, perhaps complementary to other potential
65 weakening mechanisms such as shear heating^{30,31}, reaction-induced weakening³², or the presence
66 of preexisting weak zones or viscous anisotropy^{33,34}. Here, we present a 2D thermo-mechanical
67 numerical model with a composite diffusion-dislocation creep flow law coupled to a self-
68 consistent grain size evolution model based on the paleowattmeter³⁵. Such a model allows us to
69 estimate apparent grain size distribution and the dominant deformation mechanism within the
70 upper mantle, and to investigate the importance of grain size evolution for strain localization in
71 the lithosphere during continental rifting. We test the influence of water content in the mantle
72 which affects both its viscosity and rate of grain growth. Furthermore, the effect of localized
73 grain-size-dependent weakening on the long-term strength and elastic thickness of continental
74 lithosphere is investigated and compared to pure dislocation creep experiments.

75

76 **Coupled grain size evolution thermo-mechanical model of upper mantle dynamics**

77 We apply a finite difference thermo-mechanical numerical model^{36,37} of the upper mantle
78 and crust with an Eulerian domain of 1000 x 670 km that undergoes horizontal divergence at a
79 constant total rate of 1 cm/yr. The model employs a visco-elasto-plastic rheology where the
80 viscous strain rate is composed of both dislocation and diffusion creep for constant water
81 content¹² and stresses are capped depending on the Drucker-Prager yield criterion (see Methods
82 and Supplementary Methods). The applied fluid contents in the mantle are $C_{OH} = 50\text{--}2500$
83 $H/10^6Si$, which cover the range of estimated values obtained from experimental studies^{38,39}.

84 Olivine grain size is calculated based on the paleowattmeter³⁵, which introduces a grain size
85 evolution rate composed of independent growth and reduction terms (see Methods). Grain size
86 reduction occurs by the process of dynamic recrystallization during dislocation creep, whereas
87 grain size during diffusion creep is controlled by the process of grain growth⁴⁰. Based on grain
88 sizes from experimentally deformed olivine aggregates, the fraction of work that goes into grain
89 size reduction during dynamic recrystallization is estimated to be $\lambda = 0.01$ (see Supplementary
90 Methods). The grain growth parameters we implement are derived from experiments on natural
91 olivine aggregates with in-situ water contents⁴¹ that predict significantly slower grain growth
92 than previous constraints from experiments on water-saturated, synthetic olivine⁴². Due to high
93 temperatures and thus fast growth rates, the initial grain sizes in the lower part of the model
94 domain rapidly adjust to a steady-state grain size. On the other hand, initial grain sizes within the
95 lithosphere are mainly driven by the reduction term due to lower temperatures and higher
96 deviatoric stresses.

97

98 **Rheological implications and formation of lithospheric shear zones**

99 Composite diffusion-dislocation creep numerical experiments were conducted with
100 variable water content in the mantle ($C_{\text{OH}} = 50, 175, 600, \text{ and } 2500 \text{ H}/10^6\text{Si}$) that affect both
101 viscous creep and grain growth. Mantle viscosities of the reference model ($C_{\text{OH}} = 600 \text{ H}/10^6\text{Si}$)
102 show values of $10^{19}\text{--}10^{21} \text{ Pa}\cdot\text{s}$ for the asthenosphere after 5 Myr of divergence (Fig. 1a). At 10
103 Myr, lithospheric thinning and related temperature increase below the rifted region lead to
104 viscosities as low as $5\cdot 10^{17} \text{ Pa}\cdot\text{s}$, relatively fast velocities, and gravitationally-induced
105 lithospheric dripping. After 15 and 20 Myr of divergence, asthenospheric viscosities remain
106 within $10^{18}\text{--}10^{21} \text{ Pa}\cdot\text{s}$, with lower values where fast velocities occur due to thermally- and

107 gravitationally-induced lithospheric erosion (Fig. 1a). Away from the rift, the lithosphere
108 remains intact and strong.

109 Illustrations of the dominant deformation mechanism (dislocation vs. diffusion creep) and
110 contours of grain size in the mantle demonstrate that localization of stress in the centre of the
111 model domain leads to grain size reduction and the activation of diffusion creep along large-scale
112 lithospheric shear zones (Fig. 1b). The large shear zones retain relatively small grain sizes and
113 remain dominated by diffusion creep even after 15 to 20 Myr of divergence, when a mid-ocean
114 spreading centre is established, consuming most of the extensional velocity.

115 For all experiments, grain sizes vary spatially throughout the model domain; furthermore,
116 their values are strongly sensitive implemented mantle water content. Vertical grain size profiles
117 along the side of the domain (at 5 Myr), away from the extensional zone, show values of 0.3–3
118 mm at the Moho (depending on C_{OH}) that increase to 6–15 cm at the LAB, and decrease to 2–7
119 cm at the base of the upper mantle (Fig. 2a). Grain sizes within localizing shear zones in the
120 uppermost lithosphere at 40 km depth ($y = 50$ km) show a rapid initial decrease to 60–250 μm
121 (Fig. 2b). Depending on the water content in the mantle, they are able to recover after ~ 15 Myr
122 ($C_{OH} = 2500 \text{ H}/10^6\text{Si}$) or ~ 20 Myr ($C_{OH} = 600 \text{ H}/10^6\text{Si}$). Lower water content hampers
123 substantial grain growth within previously active shear zones before 40 Myr. Average upper
124 mantle grain sizes below 300 km depth establish within ~ 2 Myr and range in between 3–12 cm
125 (Fig. 2c). Further undulations in average mantle grain size result from the downwelling of small-
126 grain-size lithospheric driplets.

127 Figure 3 shows the portions of accumulated finite viscous strain within the mantle
128 accommodated by diffusion and dislocation creep after 20 Myr of divergence. Dislocation creep
129 is the dominant deformation mechanism in large parts of the upper mantle, independent of water

130 content. Diffusion creep dominates within lithospheric shear zones that form in the early stages
131 of rifting (Fig. 1b) and assist in lithospheric dripping (Fig. 3b-d). The continental lithospheric
132 thickness defined by its viscosity varies between 90–150 km, depending on water content (Fig.
133 3).

134

135 **Effects of grain size on lithospheric strength**

136 The importance of a self-consistent grain size distribution for upper mantle dynamics
137 becomes evident when comparing our results to numerical experiments with pure dislocation
138 creep of olivine or composite diffusion-dislocation creep with a constant grain size throughout
139 the entire upper mantle. Experiments with dry dislocation creep result in extensive brittle-plastic
140 deformation of the lithosphere^{43,44}. Experiments with composite diffusion-dislocation creep and
141 small constant grain size (1 mm) results in a lithosphere thinned by convective erosion (<90 km)
142 driven by low asthenosphere viscosities of $<10^{18}$ Pa·s^{16,45}. For constant grain sizes larger than 1
143 cm, dislocation creep becomes the main deformation mechanism throughout the entire upper
144 mantle¹⁶. These numerical experiments fail to match the effective elastic lithospheric thicknesses
145 necessary to sustain orogens⁴, while brittle deformation in the lithosphere remains absent⁶. On
146 the other hand, our implementation of a self-consistent grain size evolution is able to resolve this
147 obstacle. Observed lithospheric thicknesses vary between 90–150 km (Fig. 3), while localization
148 of deformation in the lithosphere rapidly leads to grain size reduction, diffusion creep activation,
149 and related stress drop below the frictional yield, omitting failure. The diffusion-creep-related
150 stress drop furthermore reduces and replaces the importance of shear heating along lithospheric
151 shear zones^{30,46}.

152 The temporal evolution of the vertically integrated strength illustrates that experiments
153 with composite diffusion-dislocation creep coupled to a self-consistent grain size evolution show
154 a decrease of boundary forces below 5 TN/m within 1–2 Myr, while pure dislocation creep
155 experiments remain above 10 TN/m for at least ~15 Myr (Fig. 4a). Typical forces along plate
156 boundaries are on the order of 1–5 TN/m^{47,48}, which is sufficient to initiate continental rifting if
157 the grain size is small enough and diffusion creep dominates deformation²⁶. Vertical strength
158 profiles indicate that most of the strength of coupled experiments remains within the crust with
159 maximal values of ~200 MPa, while pure dislocation creep experiments exhibit at least 10 km of
160 brittle-plastic mantle lithosphere with differential stresses up to ~600–700 MPa (Fig. 4b).
161 Differential stresses of ~200 MPa close to the Moho in composite diffusion-dislocation creep
162 experiments stand in contrast to significantly lower strength along a lithospheric shear zone after
163 5 Myr (Fig. 4c). There, values of 1–10 MPa are defined by grain sizes as small as 100 μm and
164 diffusion creep as the consequent deformation mechanism, efficiently weakening the entire
165 lithospheric rift system.

166 Water content in the upper mantle has important implications for the relationships
167 between viscous flow and seismic anisotropy³⁹, hydrous melting⁴⁹, and the distribution of
168 geochemical reservoirs⁵⁰. The strength of olivine in the presence of water is significantly
169 reduced^{38,51}, as expressed in the flow law we apply here¹². Furthermore, increased water content
170 results in faster olivine grain growth⁴¹. The combined increase in grain growth rate and decrease
171 in flow stress associated with higher water contents in our experiments leads to lower
172 asthenospheric viscosity and increased thermal erosion of the lithosphere driven by diffusion
173 creep (Fig. 3).

174 The numerically predicted olivine grain size in the upper lithosphere away from shear
175 zones (0.5–10 mm; Fig. 2a) is in agreement with naturally measured values from exhumed
176 xenoliths^{18,52-54}. Furthermore, recrystallized grain sizes of 10–100 μm from localized lithospheric
177 shear zones⁵⁵⁻⁵⁸ match the grain sizes established in the diffusion-creep-dominated numerical
178 shear zones for water contents $>175 \text{ H}/10^6\text{Si}$ (Fig. 2b). There are only a few constraints on grain
179 size in the lower part of the upper mantle. However, Faul and Jackson¹⁷ suggested that the
180 seismic signature of the upper mantle low velocity zone (LVZ) may be explained with a grain
181 size of 5 cm together with the presence of fluids, which is consistent with our numerical results
182 (Fig. 2a, b).

183 In summary, presented numerical results are able to reproduce naturally observed
184 distributions of olivine grain size, which indicate that dislocation creep is the dominant
185 deformation mechanism in the upper mantle except along lithospheric shear zones, where
186 diffusion creep is activated as a result of grain size reduction by earlier dislocation creep at high
187 stress. The intrinsic weakness of such shear zones furthermore reduces the necessary boundary
188 force to initiate continental rifting. Furthermore, the long-term low viscosity lithospheric shear
189 zones allows for stretching of the continental crust and the formation of hyper-extended
190 margins⁵⁹ (Fig. 1b).

191

192 **Methods**

193 Numerical experiments were conducted with a finite difference thermo-mechanical
194 numerical code with a fully staggered Eulerian grid and a Lagrangian particle field^{36,37}. Initial
195 particle distribution in the Eulerian domain of 1000 x 670 km describes from top to bottom 10
196 km of sticky-air, 33 km of continental crust, and 627 km of upper mantle. The viscous part of the

197 strain rate is composed of both dislocation and diffusion creep¹² (see Supplementary Methods).
198 We implemented viscous flow laws defined for constant fluid contents and applied values of C_{OH}
199 = 50, 175, 600, or 2500 H/10⁶Si, which represent experimentally observed values^{38,39}. Stresses
200 are capped depending on the Drucker-Prager yield criterion to mimic brittle processes in the
201 upper lithosphere (see Supplementary Methods). The initial temperature distribution describes a
202 linear increase from 0°C at the surface ($y = 10$ km) to 660°C at the Moho ($y = 43$ km), and from
203 there to 1345°C at the thermally-induced lithosphere-asthenosphere boundary (LAB) at 150 km
204 depth ($y = 160$ km). Below the LAB, a static temperature increase of 0.5°/km is introduced.

205 Grain size of olivine is calculated based on the paleowattmeter³⁵, while all other rock
206 types exhibit a constant grain size of 1 mm. A grain size evolution rate composed of the
207 independent growth and reduction terms is introduced instead of applying a steady-state grain
208 size, which would impose an immediate, time-independent equilibration of grain size. If
209 dislocation creep dominates deformation, grain size is mainly defined by dynamic
210 recrystallization, whereas grain size during diffusion creep is determined by grain growth⁴⁰.
211 Therefore, only mechanical work related to dislocation creep ($\sigma\dot{\epsilon}_{disl}$) adds to grain size reduction
212 rate³⁵

$$213 \quad \dot{d}_{red} = \frac{\sigma\dot{\epsilon}_{disl}\lambda d^2}{c\gamma}, \quad (1)$$

214 where σ is stress, $\dot{\epsilon}_{disl}$ is dislocation creep strain rate, c is a geometric constant (π for spheric
215 grains), γ is the grain boundary energy (1.4 for olivine⁶⁰), and λ denotes the fraction of work that
216 goes into grain size reduction, whereas the rest of the work goes into the shear heating term⁶¹⁻⁶³.

217 A fitting of experimentally-derived olivine grain sizes versus expected grain size according to
218 the paleowattmeter resulted in a λ of 0.01 (see Supplementary Methods).

219 Grain growth follows a normal relationship with a grain growth rate of

$$220 \dot{d}_{gr} = K_g fH_2O \exp\left(-\frac{E_g + P \cdot V_g}{RT}\right) p^{-1} d^{1-p}, \quad (2)$$

221 where K_g is the rate constant, fH_2O is water fugacity (here as constant water content C_{OH}), E_g is
222 the activation energy, V_g the activation volume, P is pressure, T is temperature, R is the gas
223 constant, d is grain size, and p the growth exponent. We applied experimentally derived olivine
224 grain growth parameters by Speciale et al.⁴¹ that result in significantly slower grain growth than
225 previous constraints⁴².

226 Initial grain size distribution within the mantle logarithmically increases from 5 mm at
227 the Moho to 10 cm at the LAB, at which size it remains farther down. High temperatures and fast
228 growth rates in the lower part of the model domain leads to rapidly adjusting grain sizes.
229 However, grain sizes within the lithosphere are mainly dependent on the reduction term due to
230 lower temperatures and higher stresses. As a consequence, initial grain sizes in the lithosphere
231 should be large enough to initially reduce. Several initial grain size distributions were tested. See
232 Supplementary Methods for details on initial grain size distribution.

233

234 **References**

- 235 1 Karato, S. Rheology of the deep upper mantle and its implications for the preservation of
236 the continental roots: A review. *Tectonophysics* **481**, 82-98 (2010).
- 237 2 Ranalli, G. Rheology of the lithosphere in space and time. *J Geol Soc London* **121**, 19-37
238 (1997).

- 239 3 Watts, A. B. *Isostasy and Flexure of the Lithosphere*. (Cambridge University Press,
240 2001).
- 241 4 Burov, E. B. & Watts, A. B. The long-term strength of continental lithosphere: "jelly
242 sandwich" or "crème brûlée"? *GSA Today* **16**, 4 (2006).
- 243 5 Jackson, J. A. Strength of the continental lithosphere: time to abandon the jelly
244 sandwich? *GSA Today* **12**, 4-10 (2002).
- 245 6 Maggi, A., Jackson, J. A., McKenzie, D. & Priestley, K. Earthquake focal depths,
246 effective elastic thickness, and the strength of the continental lithosphere. *Geology* **28**,
247 495-498, doi:Doi 10.1130/0091-7613(2000)28<495:Efdeet>2.0.Co;2 (2000).
- 248 7 Jin, D. H., Karato, S. & Obata, M. Mechanisms of shear localization in the continental
249 lithosphere: Inference from the deformation microstructures of peridotites from the Ivrea
250 zone, northwestern Italy. *J Struct Geol* **20**, 195-209 (1998).
- 251 8 Gung, Y. C., Panning, M. & Romanowicz, B. Global anisotropy and the thickness of
252 continents. *Nature* **422**, 707-711 (2003).
- 253 9 Miyazaki, T., Sueyoshi, K. & Hiraga, T. Olivine crystals align during diffusion creep of
254 Earth's upper mantle. *Nature* **502**, 321-+ (2013).
- 255 10 Sundberg, M. & Cooper, R. F. Crystallographic preferred orientation produced by
256 diffusional creep of harzburgite: Effects of chemical interactions among phases during
257 plastic flow. *J Geophys Res-Sol Ea* **113** (2008).
- 258 11 Faul, U. H. & Jackson, I. Diffusion creep of dry, melt-free olivine. *J Geophys Res-Sol Ea*
259 **112** (2007).

- 260 12 Hirth, G. & Kohlstedt, D. Rheology of the upper mantle and the mantle wedge: A view
261 from the experimentalists. *Geophysical Monograph-American Geophysical Union* **138**,
262 83-106 (2003).
- 263 13 Jain, C., Korenaga, J. & Karato, S. I. On the Grain Size Sensitivity of Olivine Rheology.
264 *J Geophys Res-Sol Ea* **123**, 674-688 (2018).
- 265 14 Karato, S. & Wu, P. Rheology of the Upper Mantle - a Synthesis. *Science* **260**, 771-778
266 (1993).
- 267 15 Evans, B., Renner, J. & Hirth, G. A few remarks on the kinetics of static grain growth in
268 rocks. *Int J Earth Sci* **90**, 88-103 (2001).
- 269 16 Liao, J., Wang, Q., Gerya, T. & Ballmer, M. D. Modeling Craton Destruction by
270 Hydration-Induced Weakening of the Upper Mantle. *J Geophys Res-Sol Ea* **122**, 7449-
271 7466 (2017).
- 272 17 Faul, U. H. & Jackson, I. The seismological signature of temperature and grain size
273 variations in the upper mantle. *Earth Planet Sc Lett* **234**, 119-134 (2005).
- 274 18 Ave Lallemand, H. G., Mercier, J. C. C., Carter, N. L. & Ross, J. V. Rheology of the
275 Upper Mantle - Inferences from Peridotite Xenoliths. *Tectonophysics* **70**, 85-113 (1980).
- 276 19 Bernard, R. E., Behr, W. M., Becker, T. W. & Young, D. J. Relationships Between
277 Olivine CPO and Deformation Parameters in Naturally Deformed Rocks and Implications
278 for Mantle Seismic Anisotropy. *Geochemistry Geophysics Geosystems* **20**, 3469-3494
279 (2019).
- 280 20 Drury, M. R., Ave Lallemand, H. G., Pennock, G. M. & Palasse, L. N. Crystal preferred
281 orientation in peridotite ultramylonites deformed by grain size sensitive creep, Etang de
282 Lers, Pyrenees, France. *J Struct Geol* **33**, 1776-1789 (2011).

- 283 21 Dygert, N., Bernard, R. E. & Behr, W. M. Great Basin Mantle Xenoliths Record Active
284 Lithospheric Downwelling Beneath Central Nevada. *Geochemistry Geophysics*
285 *Geosystems* **20**, 751-772 (2019).
- 286 22 Bercovici, D., Ricard, Y. & Richards, M. The relation between mantle dynamics and
287 plate tectonics: A primer. *Geophysical Monograph-American Geophysical Union* **121**, 5-
288 46 (2000).
- 289 23 Gurnis, M., Zhong, S. & Toth, J. in *The History and Dynamics of Global Plate Motions*
290 Vol. Geophysical Monograph 121 73-94 (American Geophysical Union, 2000).
- 291 24 Behn, M. D., Hirth, G. & Elsenbeck, J. R. Implications of grain size evolution on the
292 seismic structure of the oceanic upper mantle. *Earth Planet Sc Lett* **282**, 178-189 (2009).
- 293 25 Braun, J. *et al.* A simple parameterization of strain localization in the ductile regime due
294 to grain size reduction: A case study for olivine. *J Geophys Res-Sol Ea* **104**, 25167-25181
295 (1999).
- 296 26 Hopper, J. R. & Buck, W. R. The Initiation of Rifting at Constant Tectonic Force - Role
297 of Diffusion Creep. *J Geophys Res-Sol Ea* **98**, 16213-16221 (1993).
- 298 27 Platt, J. P. & Behr, W. M. Grainsize evolution in ductile shear zones: Implications for
299 strain localization and the strength of the lithosphere. *J Struct Geol* **33**, 537-550 (2011).
- 300 28 Rozel, A., Ricard, Y. & Bercovici, D. A thermodynamically self-consistent damage
301 equation for grain size evolution during dynamic recrystallization. *Geophys J Int* **184**,
302 719-728 (2011).
- 303 29 Schierjott, J. C., Thielmann, M., Rozel, A. B., Golabek, G. J. & Gerya, T. V. Can Grain
304 Size Reduction Initiate Transform Faults?-Insights From a 3-D Numerical Study.
305 *Tectonics* **39** (2020).

306 30 Hartz, E. H. & Podladchikov, Y. Y. Toasting the jelly sandwich: The effect of shear
307 heating on lithospheric geotherms and strength. *Geology* **36**, 331-334 (2008).

308 31 Willis, K., Houseman, G. A., Evans, L., Wright, T. & Hooper, A. Strain localization by
309 shear heating and the development of lithospheric shear zones. *Tectonophysics* **764**, 62-
310 76 (2019).

311 32 Drury, M. R., Vissers, R. L. M., Vanderwal, D. & Strating, E. H. H. Shear Localization in
312 Upper Mantle Peridotites. *Pure Appl Geophys* **137**, 439-460 (1991).

313 33 Ogawa, M. Plate-like regime of a numerically modeled thermal convection in a fluid with
314 temperature-, pressure-, and stress-history-dependent viscosity. *J Geophys Res-Sol Ea*
315 **108** (2003).

316 34 Tommasi, A. *et al.* Structural reactivation in plate tectonics controlled by olivine crystal
317 anisotropy. *Nat Geosci* **2**, 422-426 (2009).

318 35 Austin, N. & Evans, B. Paleowattmeters: A scaling relation for dynamically
319 recrystallized grain size. *Geology* **35**, 343-346 (2007).

320 36 Gerya, T. *Introduction to Numerical Geodynamic Modelling*. (Cambridge University
321 Press, 2010).

322 37 Ruh, J. B. Numerical modeling of tectonic underplating in accretionary wedge systems.
323 *Geosphere* **16**, 1385-1407 (2020).

324 38 Hirth, G. & Kohlstedt, D. Water in the oceanic upper mantle: Implications for rheology,
325 melt extraction and the evolution of the lithosphere. *Earth Planet Sc Lett* **144**, 93-108
326 (1996).

327 39 Jung, H. & Karato, S. I. Effects of water on dynamically recrystallized grain-size of
328 olivine. *J Struct Geol* **23**, 1337-1344 (2001).

329 40 Shimizu, I. Theories and applicability of grain size piezometers: The role of dynamic
330 recrystallization mechanisms. *J Struct Geol* **30**, 899-917 (2008).

331 41 Speciale, P. A., Behr, W. M., Hirth, G. & Tople, L. Rates of Olivine Grain Growth
332 During Dynamic Recrystallization and Postdeformation Annealing. *J Geophys Res-Sol*
333 *Ea* **125** (2020).

334 42 Karato, S. Grain-Growth Kinetics in Olivine Aggregates. *Tectonophysics* **168**, 255-273
335 (1989).

336 43 Hansen, D. L. & Nielsen, S. B. Why rifts invert in compression. *Tectonophysics* **373**, 5-
337 24, doi:10.1016/S0040-1951(03)00280-4 (2003).

338 44 Jammes, S. & Huismans, R. S. Structural styles of mountain building: Controls of
339 lithospheric rheologic stratification and extensional inheritance. *J Geophys Res-Sol Ea*
340 **117**, doi:Artn B10403
341 10.1029/2012jb009376 (2012).

342 45 Candiotti, L. G., Schmalholz, S. M. & Duretz, T. Impact of upper mantle convection on
343 lithosphere hyperextension and subsequent horizontally forced subduction initiation.
344 *Solid Earth* **11**, 2327-2357 (2020).

345 46 Kiss, D., Candiotti, L. G., Duretz, T. & Schmalholz, S. M. Thermal softening induced
346 subduction initiation at a passive margin. *Geophys J Int* **220**, 2068-2073 (2020).

347 47 Bird, P., Liu, Z. & Rucker, W. K. Stresses that drive the plates from below: Definitions,
348 computational path, model optimization, and error analysis. *J Geophys Res-Sol Ea* **113**
349 (2008).

350 48 Gurnis, M., Hall, C. & Lavier, L. Evolving force balance during incipient subduction.
351 *Geochemistry Geophysics Geosystems* **5** (2004).

352 49 Katz, R. F., Spiegelman, M. & Langmuir, C. H. A new parameterization of hydrous
353 mantle melting. *Geochemistry Geophysics Geosystems* **4** (2003).

354 50 van Keken, P. E. & Ballentine, C. J. Dynamical models of mantle volatile evolution and
355 the role of phase transitions and temperature-dependent rheology. *J Geophys Res-Sol Ea*
356 **104**, 7137-7151 (1999).

357 51 Katayama, I. & Karato, S. I. Effects of water and iron content on the rheological contrast
358 between garnet and olivine. *Phys Earth Planet In* **166**, 57-66 (2008).

359 52 Behr, W. M. & Hirth, G. Rheological properties of the mantle lid beneath the Mojave
360 region in southern California. *Earth Planet Sc Lett* **393**, 60-72 (2014).

361 53 Matysiak, A. K. & Trepmann, C. A. The deformation record of olivine in mylonitic
362 peridotites from the Finero Complex, Ivrea Zone: Separate deformation cycles during
363 exhumation. *Tectonics* **34**, 2514-2533 (2015).

364 54 Titus, S. J., Medaris, L. G., Wang, H. F. & Tikoff, B. Continuation of the San Andreas
365 fault system into the upper mantle: Evidence from spinel peridotite xenoliths in the
366 Coyote Lake basalt, central California. *Tectonophysics* **429**, 1-20 (2007).

367 55 Behr, W. M. & Smith, D. Deformation in the mantle wedge associated with Laramide
368 flat-slab subduction. *Geochemistry Geophysics Geosystems* **17**, 2643-2660 (2016).

369 56 Dijkstra, A. H., Drury, M. R., Vissers, R. L. M., Newman, J. & Van Roermund, H. L. M.
370 in *Flow Processes in Faults and Shear Zones* Vol. Special Publications 224 (eds G. I.
371 Alsop, R. E. Holdsworth, K. J. W. McCaffrey, & M. Hand) 11-24 (Geological Society,
372 2004).

373 57 Precigout, J., Gueydan, F., Gapais, D., Garrido, C. J. & Essaifi, A. Strain localisation in
374 the subcontinental mantle - a ductile alternative to the brittle mantle. *Tectonophysics* **445**,
375 318-336 (2007).

376 58 Warren, J. M. & Hirth, G. Grain size sensitive deformation mechanisms in naturally
377 deformed peridotites. *Earth Planet Sc Lett* **248**, 438-450 (2006).

378 59 Péron-Pinvidic, G. & Manatschal, G. From microcontinents to extensional allochthons:
379 witnesses of how continents rift and break apart? **16**, 189-197, doi:10.1144/1354-
380 079309-903 %J Petroleum Geoscience (2010).

381 60 Duyster, J. & Stockhert, B. Grain boundary energies in olivine derived from natural
382 microstructures. *Contrib Mineral Petr* **140**, 567-576 (2001).

383 61 Austin, N. & Evans, B. The kinetics of microstructural evolution during deformation of
384 calcite. *J Geophys Res-Sol Ea* **114** (2009).

385 62 Poliak, E. I. & Jonas, J. J. A one-parameter approach to determining the critical
386 conditions for the initiation of dynamic recrystallization. *Acta Mater* **44**, 127-136 (1996).

387 63 Rosakis, P., Rosakis, A. J., Ravichandran, G. & Hodowany, J. A thermodynamic internal
388 variable model for the partition of plastic work into heat and stored energy in metals. *J*
389 *Mech Phys Solids* **48**, 581-607 (2000).

390

391 **Figure captions**

392

393 **Figure 1.** Temporal evolution of the experiment with $C_{OH} = 600 \text{ H}/10^6\text{Si}$. (a) Viscosity of upper
394 mantle and marker composition of crust. White lines denote isotherms up to 1300°C. (b)

395 Deformation mechanism in the uppermost mantle and composition of crust. Red: Diffusion
396 creep. White: Dislocation creep. Blue contours indicate grain size.

397

398 **Figure 2.** Grain sizes in the mantle at variable water content. (a) Vertical profile at $x = 990$ km
399 after 5 Myr. (b) Temporal evolution lithospheric shear zones at $y = 50$ km. (c) Temporal
400 evolution of average lower upper mantle below 300 km depth.

401

402 **Figure 3.** Percentage of finite strain accumulated by diffusion creep (blue) or dislocation creep
403 (white) after 20 Myr of divergence. Red: Contour of $\eta = 10^{21.5}$ Pa·s indicating thickness of the
404 elastic lithosphere. (a) $C_{OH} = 50$ H/ 10^6 Si. (b) $C_{OH} = 175$ H/ 10^6 Si. (c) $C_{OH} = 600$ H/ 10^6 Si. (d) C_{OH}
405 = 2500 H/ 10^6 Si.

406

407 **Figure 4.** Strength of the lithosphere. (a) Temporal evolution of the laterally averaged integrated
408 strength (boundary force) of pure dislocation and grain-size-dependent composite diffusion-
409 dislocation creep experiments. (b) Laterally ($x = 990$ – 1000 km) averaged lithospheric strength
410 profiles after 5 Myr. For color code see (a). (c) Strength and grain size profile along lithospheric
411 shear zone at 5 Myr. Location of profile indicated in Fig. 1b.

412

Figures

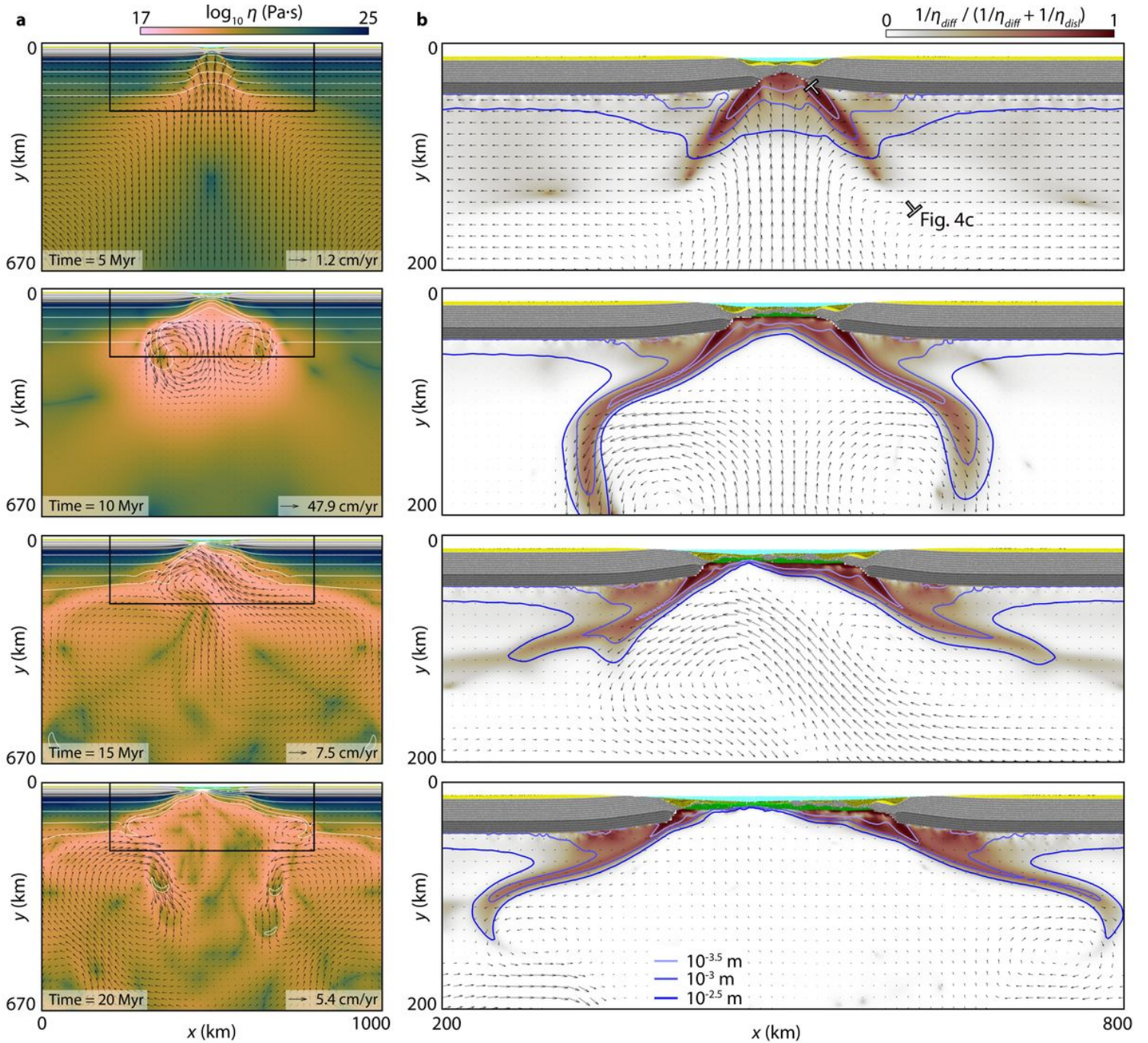


Figure 1

Temporal evolution of the experiment with $\text{COH} = 600 \text{ H}/106\text{Si}$. (a) Viscosity of upper mantle and marker composition of crust. White lines denote isotherms up to 1300°C . (b) Deformation mechanism in the uppermost mantle and composition of crust. Red: Diffusion creep. White: Dislocation creep. Blue contours indicate grain size.

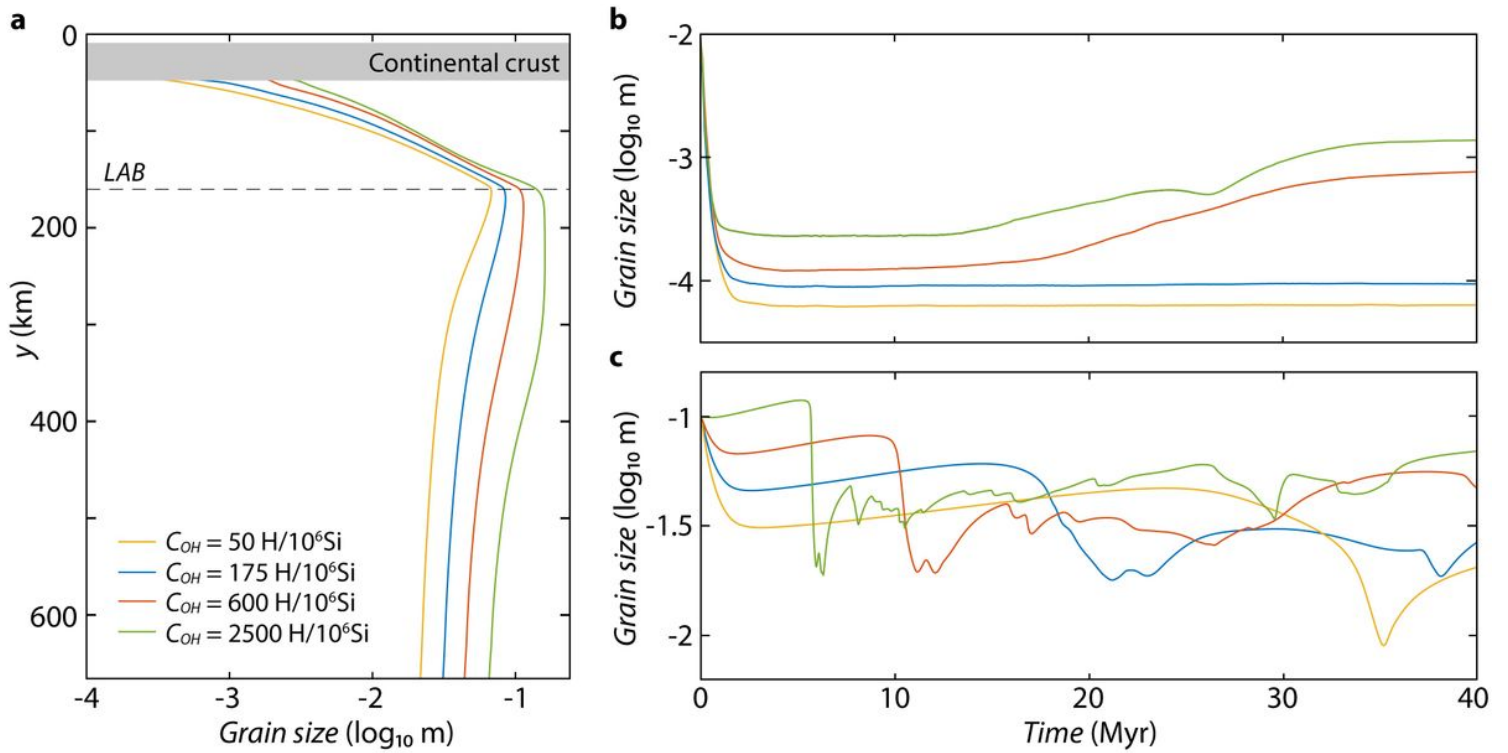


Figure 2

Grain sizes in the mantle at variable water content. (a) Vertical profile at $x = 990$ km after 5 Myr. (b) Temporal evolution lithospheric shear zones at $y = 50$ km. (c) Temporal evolution of average lower upper mantle below 300 km depth.

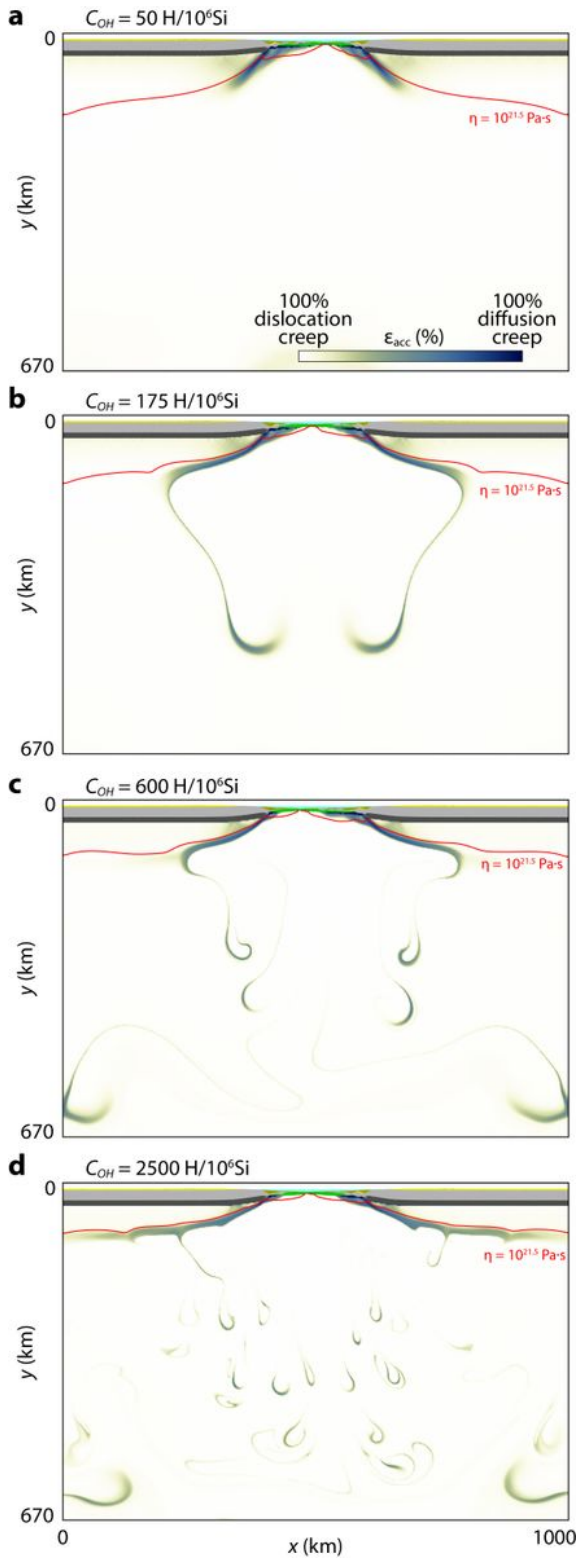


Figure 3

Percentage of finite strain accumulated by diffusion creep (blue) or dislocation creep (white) after 20 Myr of divergence. Red: Contour of $\eta = 10^{21.5} \text{ Pa}\cdot\text{s}$ indicating thickness of the elastic lithosphere. (a) $COH = 50 \text{ H}/10^6 \text{ Si}$. (b) $COH = 175 \text{ H}/10^6 \text{ Si}$. (c) $COH = 600 \text{ H}/10^6 \text{ Si}$. (d) $COH = 2500 \text{ H}/10^6 \text{ Si}$.

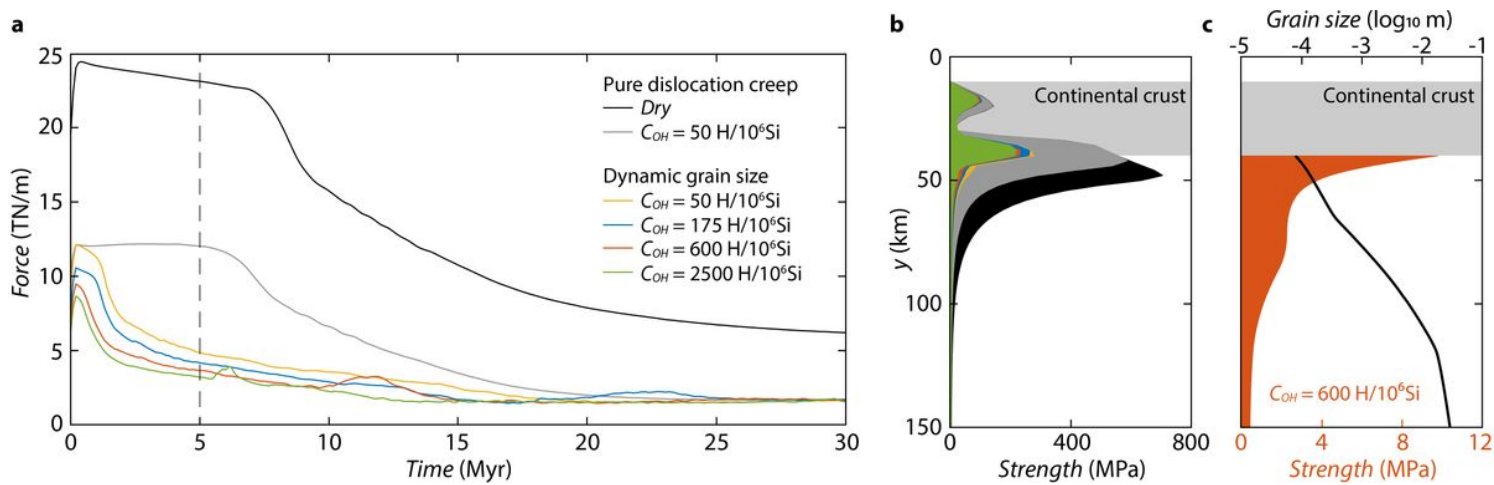


Figure 4

Strength of the lithosphere. (a) Temporal evolution of the laterally averaged integrated strength (boundary force) of pure dislocation and grain-size-dependent composite diffusion-dislocation creep experiments. (b) Laterally ($x = 990\text{--}1000 \text{ km}$) averaged lithospheric strength profiles after 5 Myr. For color code see (a). (c) Strength and grain size profile along lithospheric shear zone at 5 Myr. Location of profile indicated in Fig. 1b.

Supplementary Files

This is a list of supplementary files associated with this preprint. Click to download.

- [RuhTokleBehrSuppMat.pdf](#)
- [TableS1.xlsx](#)
- [TableS2.xlsx](#)
- [TableS3.xlsx](#)
- [TableS4.xlsx](#)